Seismoelectric wave propagation numerical modelling in partially saturated materials

S. Warden,[1] S. Garambois,[2] L. Jouniaux,[1] D. Brito,[3] P. Sailhac[1] and C. Bordes[3]

[1]*Institut de Physique du Globe de Strasbourg, CNRS UMR* 7516, *Université de Strasbourg, Strasbourg, France. E-mail: sheldon.warden@etu.unistra.fr*
[2]*ISTerre, Université Joseph Fourier, CNRS UMR* 5275, *Grenoble, France*
[3]*Laboratoire des fluides complexes et leurs réservoirs, Université de Pau et des Pays de l'Adour, CNRS UMR* 5150, *Pau, France*

SUMMARY

To better understand and interpret seismoelectric measurements acquired over vadose environments, both the existing theory and the wave propagation modelling programmes, available for saturated materials, should be extended to partial saturation conditions. We propose here an extension of Pride's equations aiming to take into account partially saturated materials, in the case of a water–air mixture. This new set of equations was incorporated into an existing seismoelectric wave propagation modelling code, originally designed for stratified saturated media. This extension concerns both the mechanical part, using a generalization of the Biot–Gassmann theory, and the electromagnetic part, for which dielectric permittivity and electrical conductivity were expressed against water saturation. The dynamic seismoelectric coupling was written as a function of the streaming potential coefficient, which depends on saturation, using four different relations derived from recent laboratory or theoretical studies. In a second part, this extended programme was used to synthesize the seismoelectric response for a layered medium consisting of a partially saturated sand overburden on top of a saturated sandstone half-space. Subsequent analysis of the modelled amplitudes suggests that the typically very weak interface response (IR) may be best recovered when the shallow layer exhibits low saturation. We also use our programme to compute the seismoelectric response of a capillary fringe between a vadose sand overburden and a saturated sand half-space. Our first modelling results suggest that the study of the seismoelectric IR may help to detect a sharp saturation contrast better than a smooth saturation transition. In our example, a saturation contrast of 50 per cent between a fully saturated sand half-space and a partially saturated shallow sand layer yields a stronger IR than a stepwise decrease in saturation.

Key words: Numerical approximations and analysis; Electrical properties; Permeability and porosity; Wave propagation; Acoustic properties.

1 INTRODUCTION

Over the past two decades, seismoelectric imaging has spawned new interest, due to theoretical advances (Pride & Morgan 1991; Pride 1994; Pride & Haartsen 1996; Haartsen & Pride 1997), modelling developments (Hu *et al.* 2007; Zyserman *et al.* 2010; Schakel *et al.* 2011, 2012; Ren *et al.* 2012; Yamazaki 2012) and a series of successful field experiments (Butler 1996; Garambois & Dietrich 2001; Thompson *et al.* 2005, 2007; Dupuis *et al.* 2007; Haines *et al.* 2007; Dupuis *et al.* 2009). In theory, the seismoelectric method could combine the sensitivity of electrical methods to hydrological properties of the subsurface, such as porosity, with a high spatial resolution comparable to that of seismic surveys (Dupuis & Butler 2006; Haines *et al.* 2007). In addition, it may also be sensitive to hydraulic permeability (Garambois & Dietrich 2002; Singer *et al.* 2005). Seismoelectric signals may have several origins, but in this work we will restrict ourselves to the study of electrokinetically in-

duced seismoelectric conversions. When a seismic wave propagates in a fluid-containing porous medium, seismoelectric signals arise from electrokinetic conversions occurring at the microscale; these signals are measurable at the macroscale, using dipole receivers either laid at the ground surface (Garambois & Dietrich 2001; Haines *et al.* 2007; Jouniaux & Ishido 2012) or deployed in boreholes (Zhu *et al.* 1999; Toksöz & Zhu 2005; Dupuis & Butler 2006; Dupuis *et al.* 2009). Several applications were foreseen for both seismoelectric and electroseismic imaging in the fields of hydrogeophysics (Dupuis *et al.* 2007) and hydrocarbon exploration (Thompson & Gist 1993; Thompson *et al.* 2007). Seismoelectric imaging may indeed be successful at characterizing high permeability fracture networks (Mikhailov *et al.* 2000; Hunt & Worthington 2000; Zhu & Toksöz 2003) and at resolving thin geological layers (Haines & Pride 2006). The theory for the coupled propagation of seismic and electromagnetic (EM) waves was reformulated by Pride (1994) for saturated porous media after previous attempts made by Frenkel

(1944) and Neev & Yeatts (1989) and has not yet been extended to partial saturation conditions. However, the full range of water saturation encountered in the near-surface should be accounted for to help interpret seismoelectric measurements acquired over partially saturated environments (Dupuis *et al.* 2007; Haines *et al.* 2007). Water content is indeed thought to influence seismoelectric waveforms via different mechanisms, the most extreme example being the absence of coseismic signals in totally dry environments (Bordes *et al.* 2009). As water content affects seismic velocity, seismic attenuation, electrical conductivity, EM propagation and diffusion, as well as the coupling coefficient, both the coseismic field and interface response (IR) properties are expected to vary with water saturation. Furthermore, saturation is also thought to control the amplitudes of seismoelectric signals generated at depth: for example, while conducting a seismoelectric survey over an unconfined aquifer, Dupuis *et al.* (2007) reported that the most prominent signal was generated at the water table, that is, at an interface displaying a large saturation contrast.

The main purpose of this work is to extend Pride's theory (Pride 1994) to unsaturated porous media. We consider here a pore space filled with a two-phase water/air mixture to investigate the seismoelectric response in vadose environments, but we hope this work will pave the way for studies in which other multiphasic pore fluids will be addressed (oil/water mixture, for example). In this paper, the parameters entering Pride's equations are explicitly described as functions of the water phase saturation S_w and the electrical formation factor F. We resort to the effective medium theory to express mechanical properties, such as the bulk and shear moduli; we also use it to derive fluid properties, such as the dynamic viscosity (Table 2). The medium's permittivity is derived using the complex refractive index method (CRIM; all acronyms used in this paper are summarized in Table 1) (Birchak *et al.* 1974), while its conductivity

is obtained by extending the conductivity derived by Pride (1994, eq. 242) to partial saturation conditions; this expression takes the surface conductivities into account. We combine this approach with the strategy introduced by Strahser *et al.* (2011), thus writing the dynamic seismoelectric coupling under partial saturation conditions as a function of the saturation-dependent streaming potential coefficient (SPC). The results obtained with four different laws describing the SPC (Perrier & Morat 2000; Guichet *et al.* 2003; Revil *et al.* 2007; Allègre *et al.* 2010) are discussed.

We also aim to provide the geophysical community with a comprehensive seismoelectric modelling programme enabling to simulate partial saturation conditions. Seismoelectric modelling programmes developed up to this day fall under one of two categories: they are either based on the general reflectivity method (Haartsen & Pride 1997; Garambois & Dietrich 2002) or they rely on finite-differences approaches (Haines & Pride 2006; Singarimbun *et al.* 2008) or finite-elements approaches (Jardani *et al.* 2010; Zyserman *et al.* 2010; Kröger & Kemna 2012). Numerical codes based on finite differences enable to model seismoelectric signals acquired over 2-D media exhibiting lateral heterogeneities, but are limited to quasi-static approximations. On the other hand, the general reflectivity method enables to model the frequency-dependent seismoelectric response but is restricted to 1-D tabular media. All these codes are dealing only with full saturation conditions. A first attempt to model electroseismic waves in sandstones saturated with two-phase oil/water or gas/water mixtures was done by Zyserman *et al.* (2010). The authors resorted to an effective medium approach to compute the mixture's mechanical properties, that is, the mechanical properties of the effective fluid were established by performing a weighted average of those of the individual fluid phases. For the electrokinetic coupling, the electrical conductivity and the dielectric permittivity, the authors retained the values taken by these parameters in the wetting phase, that is, water. Jardani *et al.* (2010) were also able to model the forward seismoelectric response over a stratified medium including a reservoir partially saturated with oil. Following the approach introduced by Revil & Linde (2006), the authors modelled the problem by solving a system of quasi-static Poisson-type equations. For a partially water-saturated reservoir, the authors replaced the excess of charges by the excess of charges divided by water saturation. Within the frame of our study, we modify the semi-analytical programme of Garambois & Dietrich (2002) to account for partial saturation conditions. We study the modelled seismic and EM velocities and quality factors and the way they vary

Table 1. Acronyms used throughout this paper.

EDL	Electrical double layer
EM	Electromagnetic
IR	Interface response
ERT	Electrical resistivity tomography
ERV	Elementary representative volume
SPC	Streaming potential coefficient
CRIM	Complex refractive index method
GPR	Ground penetrating radar

Table 2. Effective properties for a water–air mixture.

| Parameter	S_w dependence	Expression
K_f (Pa)	YES	Brie *et al.* (1995): $K_f(S_w) = (K_w - K_g)S_w^5 + K_g$
ρ_f (kg m^{-3})	YES	Arithmetic average: $\rho_f(S_w) = (1 - S_w)\rho_g + S_w\rho_w$
η (Pa s)	YES	Teja & Rice (1981): $\eta(S_w) = \eta_g(\eta_w/\eta_g)^{S_w}$
b_1 (N s m^{-1})	NO	Computed for water only with Einstein–Stokes' law.
ϵ (F m^{-1})	YES	CRIM: $\epsilon = \epsilon_0[(1 - \phi)\sqrt{\kappa_s} + \phi S_w\sqrt{\kappa_w} + \phi(1 - S_w)\sqrt{\kappa_g}]^2$
α_∞	NO	Hydraulic (geometric) tortuosity.
Λ (m)	NO	Characteristic length of the microstructure.
ω_t (rad s^{-1})	YES	$\omega_t = \frac{\eta(S_w)}{F k_0 \rho_f(S_w)}$
C_{em} and C_{os} (S)	NO	Computed for water only using Pride's expressions.
σ (S m^{-1})	YES	$\sigma(S_w, \omega) = \frac{S_w^n}{F}\sigma_w + \frac{2}{F}\frac{C_{em} + C_{os}(\omega)}{\Lambda}$

with water saturation. Three examples are presented here to illustrate seismoelectric signals variations with water saturation: the first model consists of a simple sand layer, whose saturation is allowed to vary, located on top of a saturated sandstone half-space. The second model consists of a sand layer of fixed saturation, but of varying thickness, on top of a sandstone saturated half-space. Finally, we use our modelling programme to simulate the seismoelectric response of a tabular model including a capillary fringe between an unsaturated sand overburden and a saturated half-space. This response is compared to the results obtained for a sharp saturation contrast between both units.

2 ELECTROKINETICALLY INDUCED SEISMOELECTRIC EFFECTS

The seismoelectric method relies on electrokinetically induced seismic-to-electric energy conversions occurring in fluid-containing porous media. These electrokinetic conversions are described at the microscale by the electrical double layer (EDL) theory (Gouy 1910; Chapman 1913; Stern 1924; Overbeek 1952; Dukhin & Derjaguin 1974; Davis *et al.* 1978), which subdivides the pore fluid near the fluid/solid interface in a 'bound' layer where the charges in the electrolyte are adsorbed along the pore wall, and a diffuse layer, where these ions are free to move. A compressional wave travelling through such a medium creates a fluid-pressure gradient and an acceleration of the solid matrix, both of which induce a relative motion between the counter-ions in the diffuse layer and the immobile ions adsorbed at the grain surface. Counter-ions accumulate in compressional zones while bound layers are associated with zones of dilation. This charge separation at the scale of the seismic wavelet creates an electrical potential difference known as the streaming potential. The electric field arising from this potential is known as the 'coseismic' wave, as it travels within the passing compressional seismic waves. This electric field drives a conduction current that exactly balances the streaming current (through electron migration), which means there is no electric current within a compressional seismic wave travelling within a homogeneous medium. Therefore, as coseismic waves do not exist outside the seismic waves creating them, these waves may only help to characterize the medium near the receivers at the surface (Garambois & Dietrich 2001; Haines *et al.* 2007; Bordes *et al.* 2008), whereas for borehole seismoelectric measurements, they give information about the medium in the vicinity of the well (Mikhailov *et al.* 2000).

Seismoelectric conversions are given birth when a seismic wave crosses a contrast between mechanical or electrical properties (Haartsen & Pride 1997; Chen & Mu 2005; Block & Harris 2006). This creates a transient localized charge separation across the interface, which acts as a secondary source that can be approximated as an electrical dipole oscillating at the first Fresnel zone (Thompson & Gist 1993, Fig. 1). The resulting EM wave, also known as the IR, diffuses independently from the seismic wavefield: the velocity at which it travels is several orders of magnitude greater than seismic velocities. This IR may provide information about the contrasts in the medium's properties at depth. However, IRs have typically very weak amplitudes and are often concealed by the stronger coseismic signals, as well as by ambient EM noise. This is indeed one of the key limitations of the seismoelectric method, which several authors tried to handle by extracting the IR from seismoelectric recordings through the use of various filtering techniques. Power-line noise is generally dealt with through block subtraction or sinusoidal subtraction (Butler 1993; Butler & Russell 2003).
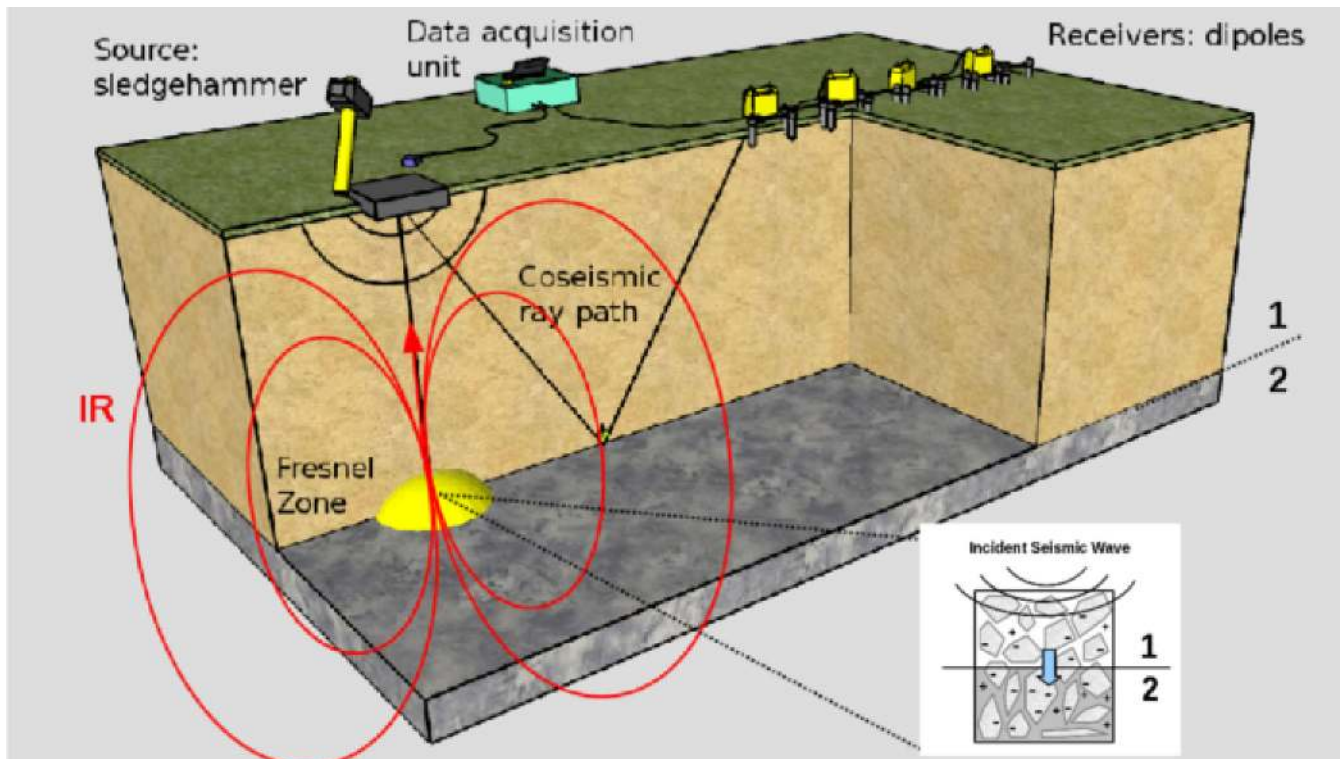
Figure 1. Typical seismoelectric survey acquisition geometry. When the incident seismic wave reaches an interface between two units of different mechanical, hydrological or electrical properties (denoted 1 and 2 in this figure), an Interface Response (IR) may arise from it. This signal originates below the shotpoint. Its radiation pattern is that of a dipole oscillating at the first Fresnel zone.

Coseismic waves are removed using dip-based techniques taking advantage of their relatively low velocity: these techniques include filtering in the frequency–wavenumber domain, Radon domain (Haines *et al.* 2007; Strahser 2007) or curvelet domain (Warden *et al.* 2012). Innovative acquisition layouts were also devised (Dupuis & Butler 2006; Haines *et al.* 2007; Dupuis *et al.* 2009), such as vertical seismoelectric profiling (VSEP): with these transmission geometries, source and receivers are placed on either side of the interface, which ensures separation between the coseismic waves and the IR.

3 SEISMOELECTRIC DEPENDENCE ON WATER SATURATION

Seismoelectric amplitude dependence on water saturation was recently investigated by Strahser *et al.* (2011) for coseismic signals. Over several months, the authors repeatedly measured the coseismic seismoelectric signals at the same locations, while monitoring the seasonal water content variations through electrical resistivity tomography, or ERT. In their work, a mixture of water and air was considered filling the pore space. They used Archie's second law, linking the conductivity of the rock σ (S m^{-1}) with the fluid's conductivity σ_{w} (S m^{-1}), the porosity ϕ and the fluid saturation S_{w}

$$\sigma = \phi^m S_{\mathrm{w}}^n \sigma_{\mathrm{w}}. \tag{1}$$

In eq. (1), m and n are the dimensionless Archie exponents, respectively, referred to as the cementation and saturation exponents. The authors expressed the normalized seismoelectric field as a power law of the effective saturation.

$$\mathbf{E} \simeq C_{\mathrm{sat}} S_{\mathrm{e}}^{(0.42 \pm 0.25)n} \rho_{\mathrm{w}} \ddot{\mathbf{u}}. \tag{2}$$

In eq. (2), $\mathbf{E}$ (V m^{-1}) is the longitudinal coseismic electric field and $\ddot{\mathbf{u}}$ (m s^{-2}) is the horizontal acceleration. C_{sat} is the steady-state SPC; ρ_{w} (kg m^{-3}) is the pore fluid's mass density. S_{e} denotes the effective saturation, defined as

$$S_{\mathrm{e}} = \frac{S_{\mathrm{w}} - S_{\mathrm{wr}}}{1 - S_{\mathrm{wr}}}, \tag{3}$$

where S_{wr} is the 'residual' saturation. An issue with this experiment is that only a limited range of saturations was investigated, as well as a single type of material, thus making it impossible to derive a universal law describing the behaviour of seismoelectric amplitudes. To overcome these *in situ* natural limitations, laboratory experiments were conducted in controlled materials to quantify the influence of water saturation on the steady-state SPC responsible of Spontaneous Potential amplitudes (Perrier & Morat 2000; Guichet *et al.* 2003; Jackson 2010; Vinogradov & Jackson 2011). Several studies (Perrier & Morat 2000; Guichet *et al.* 2003; Revil *et al.* 2007) describe the behaviour of the SPC in unsaturated conditions as a power law of the effective saturation, with the SPC monotonically increasing with saturation (see Table 3). However, recent experimental results by Allègre *et al.* (2010, 2012) suggest a more complex non-monotonic behaviour for this coefficient.

4 EXTENDING PRIDE's THEORY TO UNSATURATED CONDITIONS

4.1 A strategy combining an effective medium approach with SPC laws

The equations governing the coupled seismic and EM wave propagation in fluid-filled porous media were derived by Pride (1994) by

Table 3. Streaming potential coefficient (SPC) laws analysed throughout this study. $S(S_{\mathrm{w}})$: function of saturation appearing in eq. (17). S_{wr} denotes the residual saturation. n is Archie's saturation exponent.

Reference	$S(S_{\mathrm{w}})$	S_{wr}
Perrier & Morat (2000)	$\frac{1}{S_{\mathrm{w}}^n}\left(\frac{S_{\mathrm{w}} - S_{\mathrm{wr}}}{1 - S_{\mathrm{wr}}}\right)^2$	0.10
Guichet *et al.* (2003)	$\left(\frac{S_{\mathrm{w}} - S_{\mathrm{wr}}}{1 - S_{\mathrm{wr}}}\right)$	0.10
Revil *et al.* (2007)	$\frac{1}{S_{\mathrm{w}}^{n+1}}\left(\frac{S_{\mathrm{w}} - S_{\mathrm{wr}}}{1 - S_{\mathrm{wr}}}\right)^4$	0.10
Allègre *et al.* (2010)	$\left(\frac{S_{\mathrm{w}} - S_{\mathrm{wr}}}{1 - S_{\mathrm{wr}}}\right)\left(1 + 32\left(1 - \left(\frac{S_{\mathrm{w}} - S_{\mathrm{wr}}}{1 - S_{\mathrm{wr}}}\right)\right)^{0.4}\right)$	0.305

combining Maxwell's equations with Biot's equations for poroelasticity (Biot 1956a,b). These two subsystems are coupled through two transport equations (eqs 251 and 252 in Pride 1994).

$$\mathbf{J} = \sigma(\omega)\mathbf{E} + L(\omega)\left(-\nabla p + \omega^2 \rho_{\mathrm{w}} \mathbf{u}_{\mathrm{s}}\right), \tag{4}$$

$$-\mathrm{i}\omega\mathbf{w} = L(\omega)\mathbf{E} + \frac{k(\omega)}{\eta_{\mathrm{w}}}\left(-\nabla p + \omega^2 \rho_{\mathrm{w}} \mathbf{u}_{\mathrm{s}}\right). \tag{5}$$

Both the above equations assume a e$^{-\mathrm{i}\omega t}$ time dependence of the propagating wave, where ω (rad s^{-1}) denotes the angular frequency. Eq. (4) expresses the macroscopic electrical current density $\mathbf{J}$ (A m^{-2}) as the sum of the average conduction and streaming current densities, respectively, the first and second term on the right-hand side of eq. (4). The parameter $\sigma(\omega)$ (S m^{-1}) is the frequency-dependent conductivity of the material and $\mathbf{E}$ (V m^{-1}) denotes the electric field. Streaming currents may be induced by both the pressure gradient $-\nabla p$,where p (Pa) is the pore-fluid pressure, and the acceleration of the solid frame $\omega^2 \rho_{\mathrm{w}} \mathbf{u}_{\mathrm{s}}$, where ρ_{w} (kg m^{-3}) is the density of the fluid (water) and $\mathbf{u}_{\mathrm{s}}$ (m) denotes the solid displacement. In a similar fashion, the fluid velocity $-\mathrm{i}\omega\mathbf{w}$ (m s^{-1}) is written in eq. (5) as the sum of electrically and mechanically induced contributions. The frequency-dependent permeability is written as $k(\omega)$ (m^2) and the dynamic viscosity of the fluid is expressed as η_{w} (Pa s). Special attention should be brought to the complex and frequency-dependent coupling $L(\omega)$, effectively linking eqs (4) and (5)

$$L(\omega) = L_0\left[1 - \mathrm{i}\frac{\omega}{\omega_{\mathrm{t}}}\frac{p}{4}\left(1 - 2\frac{d}{\Lambda}\right)^2\left(1 - \mathrm{i}^{3/2}d\sqrt{\frac{\omega\rho_{\mathrm{w}}}{\eta_{\mathrm{w}}}}\right)^2\right]^{-\frac{1}{2}}. \tag{6}$$

In eq. (6), Λ (m) is a geometrical parameter of the pores, defined in Johnson *et al.* (1987), whereas p is a dimensionless parameter defined as $p = \frac{\phi}{\alpha_\infty k_0}\Lambda^2$ and consisting only of the pore-space geometry terms. This parameter p was originally denoted m in Pride (1994). When k_0, ϕ, α_∞ and Λ are independently measured, m is comprised between 4 and 8 for a variety of porous media ranging for grain packing to capillary networks consisting of tubes of variable radii (Johnson *et al.* 1987). The parameter d (m) denotes the Debye length, while ω_{t} (rad s^{-1}) is the permeability-dependent transition angular frequency between the low-frequency viscous flow and high-frequency inertial flow. Finally, L_0 denotes the electrokinetic coupling, whose expression will be discussed further. This coupling $L(\omega)$ was studied by Reppert *et al.* (2001), Schoemaker *et al.* (2007), Jouniaux & Bordes (2012) and Glover *et al.* (2012). When this coefficient is set to zero, the two subsets of equations describing the behaviour of EM and seismic waves are decoupled.

As previously pinpointed, Pride's equations have not yet been extended to partial saturation conditions. However, the behaviour of seismic waves in partially saturated porous media has been thoroughly studied, notably to explain seismic attenuation and waveform (Müller *et al.* 2010). Laboratory experiments on sandstone

(Knight & Dvorkin 1992) and limestone (Cadoret *et al.* 1995) have shown that seismic attributes indeed depend on water saturation. Not only the water content, but also the way water fills the pore space influences seismic velocities, attenuation and dispersion (Knight & Nolen-Hoeksema 1990; Dvorkin & Nur 1998; Barrière *et al.* 2012). The 'patchy saturation' model accounts for the heterogeneous mesoscale fluid distribution in the pore space: according to this model, under partial saturation conditions, patches of the porous medium are filled with gas, while other patches are filled with liquid. The distribution of the patches controls to which extent the mechanical properties of the medium deviate from those predicted by the Biot–Gassman theory. A simpler approach is offered by the effective medium theory, which states that the multiphasic fluid occupying the pore space can be replaced by a homogeneous fluid of equivalent effective properties (Gueguen & Palciauskas 1994). This approach allows to apply Biot's equations as if dealing with a biphasic solid/fluid medium. We will further discuss the mixing laws used to compute the medium's effective mechanical properties as a function of water saturation in Section 4.2. The effective medium approach, however, may not be blindly applied to determine all of the medium's properties. For instance, the electrical conductivity of a water/air mixture may not be computed as the weighted average of the conductivities of each individual phase, as under partial saturation conditions, the electrical current preferentially flows in the water phase: this calls for expressions of the saturation-dependent conductivity taking the formation factor into account. We will detail the laws used to compute the medium's electrical properties in unsaturated conditions in Section 4.3, bringing special attention to their frequency validity and to the rock types to which they apply. Other parameters, such as the ionic mobilities or the Debye length are intrinsically fluid-related and lose their meaning inside the air phase. For such parameters, we have chosen to use their values at full saturation.

4.2 Mechanical and fluid properties

4.2.1 Bulk modulus

The effective bulk modulus of a water/air mixture is computed using the law proposed by Brie *et al.* (1995).

$$K_f = (K_w - K_g)S_w^e + K_g, \tag{7}$$

where the 'g' and 'w' indexes denote the gaseous (air) and liquid (water) phase, respectively. The exponent e is derived empirically. Taking e = 1 allows to simplify Brie's relation to Voigt's arithmetic average ('lower bound'), while the Reuss harmonic average ('upper bound') may be approximated by choosing e = 40 (Fig. 2). We chose to work with the exponent e = 5, as with this value Brie's law fits White's curve fairly well (Carcione *et al.* 2006). White (1975) has developed a patchy saturation model describing velocity and attenuation as a function of frequency, fluid viscosity, permeability and patch size. The author considers gas-filled spheres located inside water-filled spheres: these patches have a scale larger than the grains, but smaller than the wavelength.

4.2.2 Viscosity

We compute the effective viscosity of the water/air mixture using the formula derived by Teja & Rice (1981).
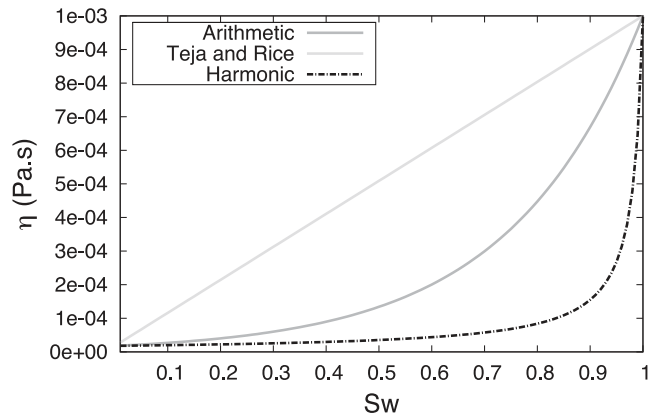
$$\eta = \eta_g \left(\frac{\eta_w}{\eta_g} \right)^{S_w}, \tag{8}$$
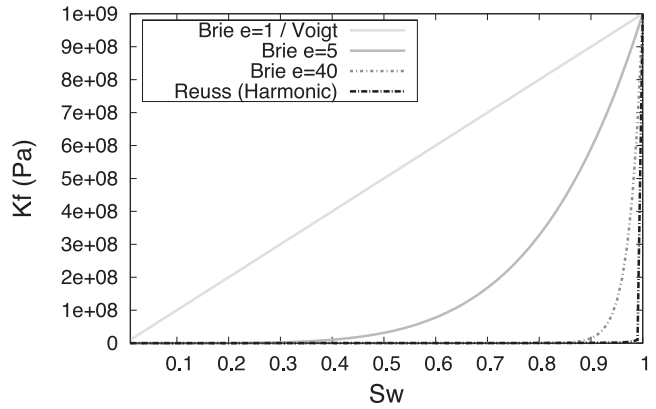
Figure 2. Effective bulk modulus K_f for a water–air mixture as a function of water saturation S_w. A water bulk modulus of $K_w = 10^9$ Pa was chosen, while a modulus of $K_g = 10^5$ Pa was taken for the gaseous phase.

Figure 3. Effective viscosity η for a water–air mixture as a function of water saturation S_w. The air and water viscosity proposed by Ritchey & Rumbaugh (1996) are used here: $\eta_g = 1.8 \times 10^{-5}$ Pa s and $\eta_w = 10^{-3}$ Pa s, respectively.

where η_g denotes the viscosity of the gaseous phase (air), while the viscosity of the liquid phase (water) is written η_w. We checked that the saturation-dependent effective viscosity obtained with this formula falls within the Voigt and Reuss bounds (Fig. 3). This effective viscosity is notably used to compute Biot's transition angular frequency ω_t between viscous and inertial flow regimes, as well as $\tilde{\rho}$, the flow resistance density term which describes the dynamic loss of energy due to the fluid flow with an explicit frequency dependence, used to compute the complex density. However, we did not use this effective viscosity in the expression of the static seismoelectric coupling L_0, for which the viscosity of water was taken instead, as we assume that the relative motion between the gaseous phase and the liquid and/or the solid phases does not create any charge separation.

4.2.3 Mass density

The effective mass density ρ is computed using the arithmetic average

$$\rho_f = S_w \rho_w + (1 - S_w)\rho_g, \tag{9}$$

where ρ_w and ρ_g denote the mass densities of water and air, given in (kg m^{-3}). We assume ambient pressure and temperature conditions,

a reasonable hypothesis regarding the depth of investigation of several tens of metres considered here. For greater depths, one would need to resort to the empirical laws expressing the mass densities as a function of temperature and pressure, such as those proposed by Batzle & Wang (1992) or Mavko *et al.* (2009).

4.3 EM properties

4.3.1 Dielectric constant

Several formulae enable to compute the dielectric constant for multiphasic media, which were notably developed for ground-penetrating radar (GPR) applications (Garambois *et al.* 2002). The CRIM formula (Birchak *et al.* 1974) is known to give good results at high frequencies, above 1000 MHz according to Gueguen & Palciauskas (1994) and above 500 MHz according to Mavko *et al.* (2009).

$$\kappa = [(1 - \phi)\sqrt{\kappa_s} + \phi S_w \sqrt{\kappa_w} + \phi(1 - S_w)\sqrt{\kappa_g}]^2. \quad (10)$$

One may argue that the CRIM formula is valid when displacement currents dominate over conduction currents, but that this may no longer be the case at seismic or seismoelectric frequencies, that is, from tens of Hertz to hundreds of Hertz. The behaviour of the dielectric constant of sandstones versus water saturation at lower frequencies was investigated by several authors, between 5 Hz and 13 MHz (Knight 1984), 60 kHz and 4 MHz (Knight & Nur 1987) and between 0.1 Hz and 100 kHz (Gomaa 2008). Several authors have also studied the behaviour of the dielectric constant in sands and sandstones depending on whether the samples are submitted to imbibition or drainage: for instance, Plug *et al.* (2007) have measured the electric permittivity for sand–water–gas systems at 100 kHz and have found that the permittivity data show hysteresis between imbibition and drainage. While the dielectric constant values measured at several water saturation levels by Knight (1984) for a Berea sandstone at 13 MHz are of the same order of magnitude as those predicted with the CRIM formula, they are much higher at lower frequencies: for example, at 57 kHz for $S_w = 0.9$, the dielectric constant is about twice the one predicted using the CRIM formula (Knight 1984). At a frequency of 100 Hz, for a saturated clay-free haematitic sandstone, Gomaa (2008) measures a relative permittivity of about 2.4×10^4, that is, more than 2000 times greater than the dielectric constant predicted by the CRIM formula on a similar sandstone. This increase of the dielectric constant with decreasing frequency could be explained by the Maxwell–Wagner relaxation model (Gueguen & Palciauskas 1994), for which the accumulation of electrical charges in the pore space is responsible for the dielectric dispersion observed at audiofrequencies. We conducted a sensitivity study for a simple half-space consisting of sands and found that increasing the dielectric constant by three orders of magnitude increased the EM wave velocity by 4 per cent, while increasing the maximum coseismic amplitude by less than 1 per cent. Following Zyserman *et al.* (2010), we chose to use the permittivity of the wetting phase, that is, water, in the expression of the seismoelectric coupling L_0: this choice considerably reduces the impact of a change in permittivity on the seismoelectric amplitudes, which was confirmed by our sensitivity study. In the following, we will work under the assumption that these Maxwell–Wagner effects do not impact seismoelectromagnetic waveforms and we will compute the medium's relative permittivity using the CRIM formula.

4.3.2 Electrical conductivity

For fully saturated media, Pride (1994, eq. 242) expressed the conductivity as

$$\sigma(\omega) = \frac{\phi \sigma_w}{\alpha_\infty} \left[1 + 2 \frac{C_{em} + C_{os}(\omega)}{\sigma_w \Lambda} \right]. \quad (11)$$

In eq. (11), C_{em} (S) is the excess conductance associated with the electromigration of double layer ions, while $C_{os}(\omega)$ (S) is the frequency-dependent electroosmotic conductance due to electrically induced streaming of the excess double-layer ions. Both conductances are of the same order of magnitude (Pride 1994). The parameter α_∞ denotes the dimensionless tortuosity. By introducing the formation factor $F = \alpha_\infty / \phi = \phi^{-m}$, one can rewrite this equation as

$$\sigma(\omega) = \phi^m \sigma_w + \frac{2}{F} \frac{C_{em} + C_{os}(\omega)}{\Lambda}. \quad (12)$$

In eq. (12), the first term denotes the volume conductivity (S m^{-1}), while the second term is the surface conductivity (S m^{-1}). To adapt this equation to partially saturated conditions, we identify its first term with the conductivity derived using Archie's second law (eq. 1)

$$\sigma(S_w, \omega) = \frac{S_w^n}{F} \sigma_w + \frac{2}{F} \frac{C_{em} + C_{os}(\omega)}{\Lambda}. \quad (13)$$

This approach combines Pride's frequency-dependent formula with Archie's law, developed under static conditions, to return conductivity as a function of both water saturation and frequency (Fig. 4). We assume here that the term $2/F \times (C_{em} + C_{os}(\omega))/\Lambda$ does not vary with water saturation S_w. According to Brovelli *et al.* (2005), the surface conductance Σ_s (S) should indeed be independent of the water saturation level. The authors explain that for $S_w \geq 0.15$, the thickness of the wetting phase at the surface of the rock matrix is greater than the Debye length, that is, greater than the EDL thickness: therefore a saturation increase does not modify the properties of the EDL. It seems reasonable to make the same hypothesis here, because this work only aims to investigate a realistic range of saturation and assumes a non-negligible residual saturation S_{wr}. To check that this residual saturation ensures the existence of the EDL, we modelled increasing saturation levels inside capillary pores which radii were comprised between 1 and 100 μm, assuming the wetting phase to grow from the pore walls towards the centre of the pore space (Allen 1996). We computed the thickness of the wetting phase (Fig. 5), which we compared to an analytical
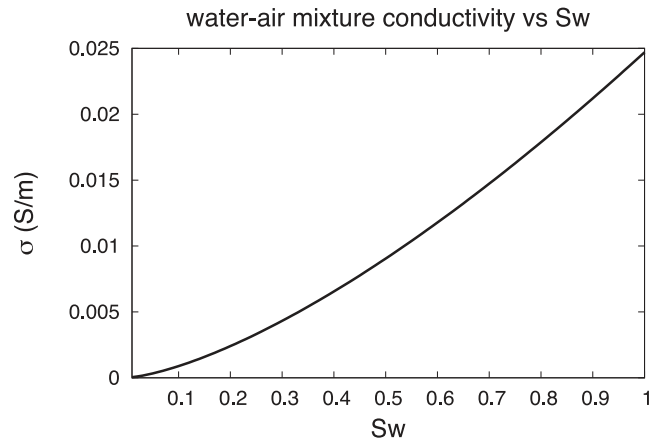
Figure 4. Electrical conductivity of the rock versus water saturation S_w, computed at 120 Hz using the equation modified from Pride (1994, eq. 13).
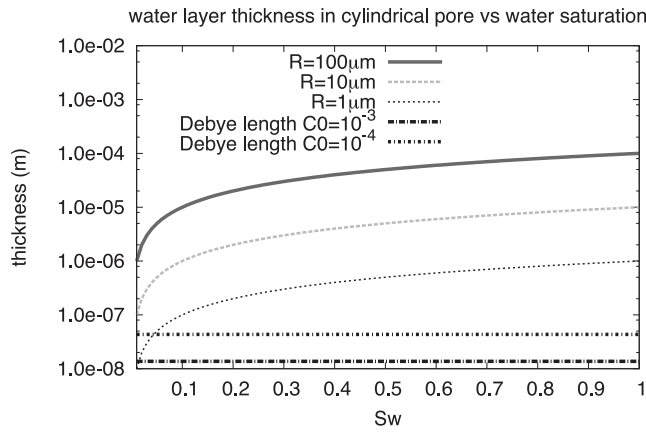
Figure 5. Comparison between the thickness of the wetting phase for cylindrical pores for various pore radii and the Debye length (m) computed for a salinity of $C_0 = 10^{-3}$ and $C_0 = 10^{-4}$ mol L^{-1}, over the entire saturation range.

expression of the Debye length given by Pride (1994). It appears that for this simple pore geometry, for a salinity higher than 10^{-4} mol L^{-1} and saturation greater than 10 per cent, the thickness of the wetting phase is always greater than the Debye length, thus allowing us to assume the surface conductivity independent from S_w.

4.4 Expressing the electrokinetic coupling as a function of the SPC

Pride (1994) defined the electrokinetic coupling L_0 at full saturation as

$$L_0 = -\frac{\phi}{\alpha_\infty} \frac{\epsilon_0 \kappa_w \zeta}{\eta_w} \left(1 - 2\frac{\tilde{d}}{\Lambda}\right). \tag{14}$$

In eq. (14), ζ denotes the zeta potential (V). The SPC C_{sat}, also defined at full saturation, is described by the Helmholz–Smoluchowski equation when the surface conductivity can be neglected with respect to the bulk conductivity (Dukhin & Derjaguin 1974).

$$C_{sat} = \frac{\epsilon_w \zeta}{\eta_w \sigma_w} = \frac{\epsilon_w \zeta}{F \eta_w \sigma}. \tag{15}$$

In eq. (15), ϵ_w (F m^{-1}), η_w (Pa s) and σ_w (S m^{-1}) are, respectively, the water permittivity, dynamic viscosity and conductivity. $\sigma = \sigma_w/F$ (S m^{-1}) is the rock effective conductivity at full saturation, deduced from Archie's law. Under full saturation conditions, the electrokinetic coupling L_0 can therefore be expressed as a function of the SPC C_{sat}

$$L_0 = -C_{sat}\sigma \left(1 - 2\frac{\tilde{d}}{\Lambda}\right). \tag{16}$$

Several authors have studied the water saturation dependence of the SPC. Perrier & Morat (2000) studied the electrical daily variations measured by independent dipoles at a test site over several weeks. These variations were interpreted as streaming potentials produced by capillary flow in the vadose zone. Since the SPC is defined as the hydraulic flow divided by the electrical flow, the authors introduced a saturation dependence of the SPC through the dependence of the hydraulic flow to water saturation, taken into account by the dimensionless relative permeability $k_r(S_w)$. Guichet *et al.* (2003) established from experimental measurements in a sand column that the SPC was either constant or decreased by a factor 3 when water saturation decreased from 100 to 40 per cent. Based

on these measurements, the authors proposed an expression for the saturation-dependent SPC. Revil *et al.* (2007) proposed an expression for the SPC in unsaturated conditions based on a theoretical approach. Considering a mixture between water and an insulating viscous fluid saturating the pore space, they used a volume-averaging approach to establish the electrical current density, as well as the filtration velocities, thus obtaining a set of macroscopic constitutive equations. Assuming the excess charge density of the pore water to increase with decreasing water saturation, they deduced an expression of the SPC depending on the relative permeability k_r and on water saturation S_w: they found an expression quite similar to the equation empirically established by Perrier & Morat (2000). The three laws mentioned above all predict a monotonic increase in the SPC with increasing water saturation. However, recent work by Allègre *et al.* (2010, 2012) suggests that the SPC could rather follow a non-monotonic behaviour with saturation. According to their observations in Fontainebleau sands, it increases when saturation decreases between 1 and 0.80–0.65, and then decreases as the water saturation decreases, thus following a 'bell-shaped' curve. All aforementioned models can be written as a product between the SPC at full saturation and a function of saturation $S(S_w)$ (Table 3):

$$C(S_w) = C_{sat}S(S_w). \tag{17}$$

To express the electrokinetic coupling L_0 under partial saturation conditions, one can substitute the SPC at full saturation in eq. (16) with the saturation-dependent SPC given in eq. (17). One also needs to replace the rock effective conductivity at full saturation in eq. (16) with a saturation-dependent effective conductivity. Using Archie's second law, that is, neglecting surface conductivities, one can rewrite $L_0(S_w)$ as

$$L_0(S_w) = -\frac{1}{F}\frac{\epsilon_w \zeta}{\eta_w}\left(1 - 2\frac{\tilde{d}}{\Lambda}\right) S_w^n S(S_w). \tag{18}$$

4.5 Validation step

The full-waveform modelling code of seismoelectromagnetic wave propagation in partially saturated conditions was derived using an extension of the saturated modelling code developed by Garambois & Dietrich (2002). Within this Fortran program, we replaced the expressions for the fluid bulk modulus, mass density, viscosity, relative dielectric permittivity and electrical conductivity with their equivalent effective expressions, as discussed in Sections 4.2, 4.3 and 4.4. Apart from these modifications, our partially saturated version includes a few minor changes with respect to the original program. For instance, we use a different definition for the ionic mobilities b_l. The saturated version relied on the value of 3×10^{11} Ns m^{-1} suggested by Pride (1994) for typical inorganic ions such as sodium. This value was multiplied by two in the expressions of the conductivities and conductance, to account for the mobility of the entire molecule. We substituted this value with an expression based on Stokes' law describing the motion of a sphere in a viscous medium (Pride & Morgan 1991; Bard & Faulkner 2001)

$$b_{li} = \frac{v_i}{6\pi \eta_w R_i}. \tag{19}$$

In eq. (19), the subscript i refers to the considered species, while v_i is its valence and R_i its ionic radius (m). According to Pride & Morgan (1991), $R_{Na+} = 1.83 \times 10^{-10}$ m for sodium and $R_{Cl-} = 1.20 \times 10^{-10}$ m for chloride. These species having a valence of 1, one finds $b_l = 7.32 \times 10^{11}$ Ns m^{-1} for a viscosity of water of 10^{-3} Pa s. The way the elastic moduli are specified in the programme

also differs from the saturated version, which required the fluid, solid and frame bulk moduli as well as the solid and frame shear moduli to be entered. Our version introduces a user-specified dimensionless consolidation parameter c_s used to compute the frame moduli from the solid grain moduli and the medium's porosity, following Pride (2005), and used for instance by Dupuy *et al.* (2011).

$$K_{\mathrm{fr}} = K_{\mathrm{s}} \frac{1 - \phi}{1 + c_s \phi} \quad (20)$$

and

$$G_{\mathrm{fr}} = G_{\mathrm{s}} \frac{1 - \phi}{1 + 1.5 c_s \phi}. \quad (21)$$

Parameters K_{fr} (Pa) and K_{s} (Pa) are the frame and solid bulk moduli, while G_{fr} (Pa) and G_{s} (Pa) denote the frame and solid shear moduli. For example, the solid shear modulus of quartz grains ($G_{\mathrm{s}} = 44 \times 10^9$ Pa), a porosity of 20 per cent and a consolidation of 20 yield a frame shear modulus G_{fr} of 5×10^9 Pa.

We compared the results obtained using both the saturated version of our programme and the version developed for partially saturated conditions, for a simple tabular model consisting of a shallow sand layer over a sandstone half-space. We computed the velocities obtained using both programmes for the fast and slow *P* waves, *S* wave and EM wave travelling inside both layers. The seismic velocities computed with our code and those returned by the original programme were identical, while for the EM velocities, the deviation remained below 0.001 per cent. We also compared the maximum, minimum and mean amplitudes of the seismoelectric signals modelled using both our programme and its original version and found the same values using either tool. The electrograms modelled using both programmes appeared almost identical, with the residual between both recordings consisting only of non-coherent residual noise whose mean amplitude is less than 1 per cent the mean amplitude of the original recording. Finally, a full reciprocity test was successfully performed on the partially saturated programme.

5 PARTIALLY SATURATED SANDY OVERBURDEN ON TOP OF A FULLY SATURATED SANDSTONE HALF-SPACE

5.1 Model description

In the previous section, we verified that for a fully saturated porous medium, our modelling programme granted the same results than the original programme in terms of velocities, quality factors and amplitudes. We now investigate the seismoelectric response modelled with this programme over the entire 'effective' saturation S_e range, that is, from the residual saturation $S_w = S_{wr}$ up to $S_w = 1$. We consider a tabular medium consisting of a 30-m thick sand layer on top of a sandstone half-space (Table 4). We allow the effective saturation in the sand overburden to vary from 0 to 1 with a 0.05 saturation increment. We model a vertical seismic source located near the surface, at a depth of 3 m, to simulate a downhole seismic gun shot. An array of 201 dipole receivers is modelled. Receivers are buried at a depth of 1 m between −50 and 50 m, with the origin set at the source location.

5.2 Velocity and attenuation analysis

We computed analytically the fast and slow *P* waves, *S* wave and EM wave velocities over the entire effective saturation range for the sand layer, using the SPC law derived by Guichet *et al.* (2003),

**Table 4.** Properties of the model described in Section 5.

	Sand	Sandstone
$\phi(\%)$	35	20
c_s	20	5
m	2.05	1.70
k_0 (m^2)	10^{-11}	10^{-13}
k_s (Pa)	35×10^9	36×10^9
G_s (Pa)	44×10^9	44×10^9
k_f (Pa)	2.27×10^9	2.27×10^9
k_{fr} (Pa)	2.84×10^9	14.40×10^9
G_{fr} (Pa)	2.49×10^9	14.08×10^9
η_{w} (Pa s)	1×10^{-3}	1×10^{-3}
η_{g} (Pa s)	1.8×10^{-5}	1.8×10^{-5}
ρ_{s} (kg m^{-3})	2.6×10^3	2.6×10^3
ρ_{w} (kg m^{-3})	1×10^3	1×10^3
ρ_{g} (kg m^{-3})	1	1
C_0 (mol L^{-1})	1×10^{-3}	1×10^{-3}
σ (S m^{-1})	1.32×10^{-3}	7.54×10^{-4}
ζ (V)	-0.065	-0.065
κ_{w}	80	80
κ_{s}	4	4
κ_{g}	1	1
T (K)	298	298

at four frequencies: 50, 100, 150 and 200 Hz (Fig. 6). Both the fast *P*-wave and *S*-wave velocities do not vary significantly with frequency over the investigated frequency range. *S*-wave velocity variations are due to saturation-related effective fluid mass density changes and are very limited: V_S (m s^{-1}) monotonically decreases between 1200 and 1100 m s^{-1} over the entire effective saturation range. On the other hand, the velocities for the Biot slow *P* wave and the EM wave are dramatically affected by the saturation level. V_{Ps} (m s^{-1}) increases from 2 to about 100 m s^{-1} over the first half of the saturation range, before decreasing by a few m s^{-1}. V_{EM} (m s^{-1}) monotonically decreases by one order of magnitude over the effective saturation range, from 3×10^6 to 3×10^5 m s^{-1} at 50 Hz. The velocities of both the Biot slow *P* wave and the EM wave are highly dispersive and frequency-dependent: the higher the frequency, the greater the velocity. We also plotted the quality factors against saturation for all four wave types, at 50, 100, 150 and 200 Hz (Fig. 7). The quality factor is defined as

$$Q = \frac{1}{2} \frac{Re(s)}{Im(s)}. \quad (22)$$

In eq. (22), s (S m^{-1}) is the slowness of the considered wave. The quality factor Q quantifies the effect of anelastic attenuation on seismic or EM waves; the smaller the quality factor, the greater the absorption. Fast *P*-wave and *S*-wave quality factors vary dramatically with the effective saturation. For instance, Q_{Pf} at 50 Hz decreases from 1.3×10^5 to about 500 when S_e increases from 0 to 0.45 before increasing again to 2.5×10^6. On the other hand, for the frequency range investigated here, the EM quality factor variations are negligible: at 200 Hz, Q_{EM} only decreases between 0.5013 and 0.5 over the entire effective saturation range. This calls for a thorough investigation of the quality factor variations with frequency. For five saturation levels (20, 40, 60, 80 and 100 per cent), we plotted the quality factors against frequency f, with f ranging between 1 and 10^8 Hz (Fig. 8). The fast *P* waves and *S* waves display a similar behaviour, dictated by the fluid flow regime. For viscous fluid flow, that is, for $f < 2\pi\omega_{\mathrm{t}}$, their quality factor decreases as ω_{t}/f: ω_{t} denotes here the angular transition frequency, defined as $(\eta S_w^m)/(Fk_0\rho_f)$. For inertial flows, that is, for $f > 2\pi\omega_{\mathrm{t}}$,
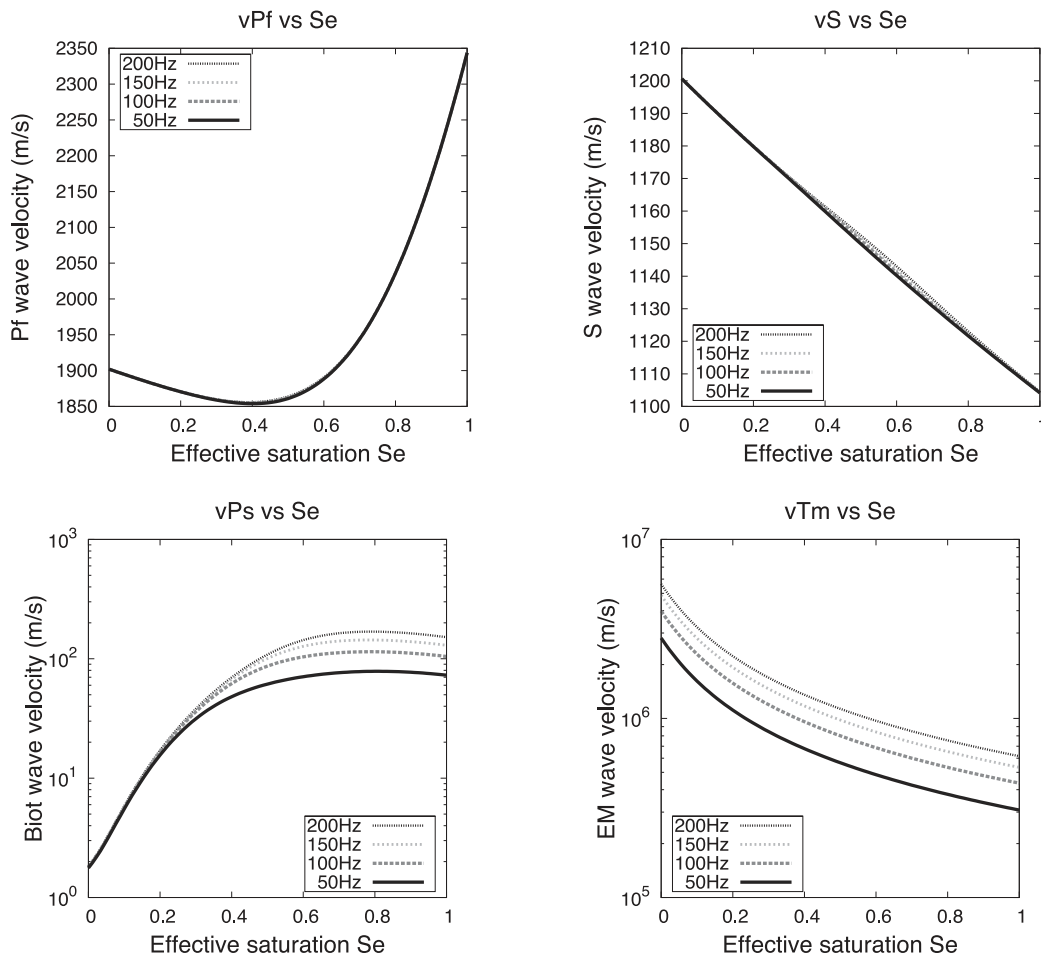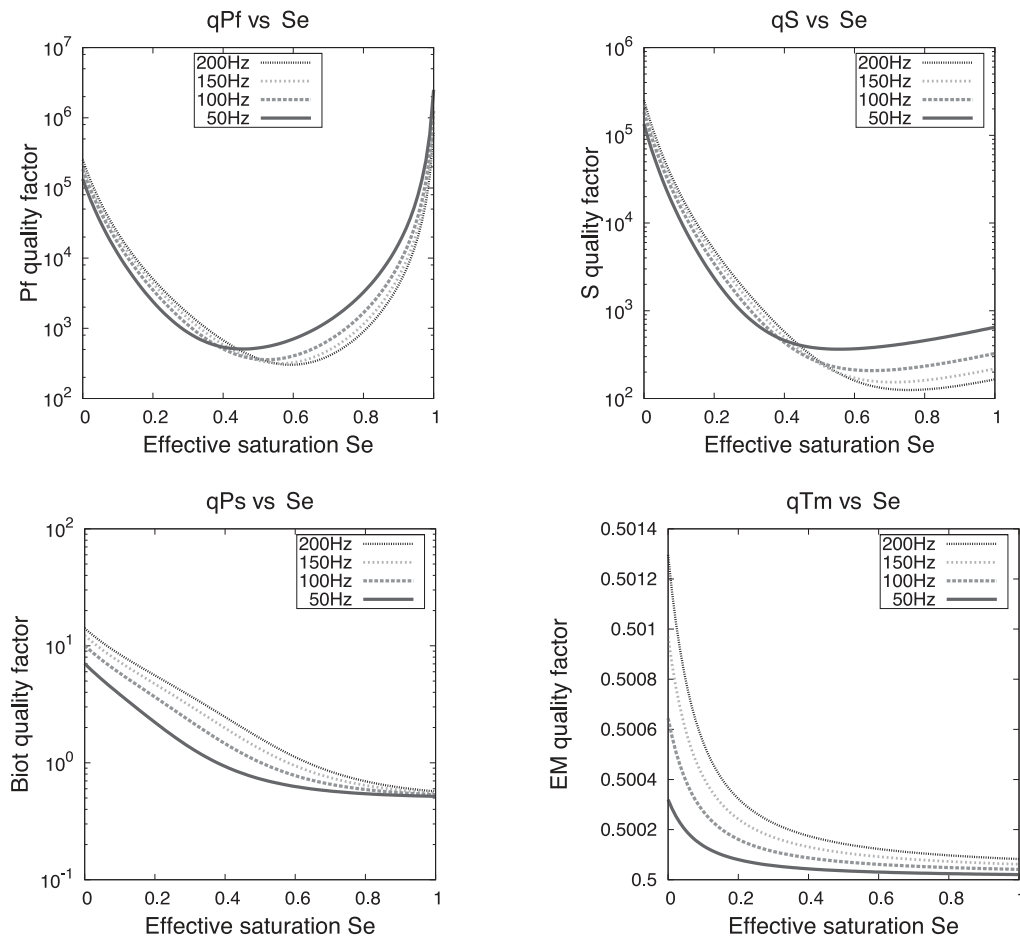
Figure 6. *P* wave, *S* wave, Biot slow wave and EM wave velocities as a function of effective saturation S_e for the sand layer described in Table 4. These velocities were computed at 50, 100, 150 and 200 Hz. Note that the *P*-wave and *S*-wave velocities are plotted with a linear scale.

Q_{Pf} and Q_S increase as $\sqrt{(f/\omega_t)}$. Therefore, attenuation is greatest when $f = 2\pi\omega_t$. It is interesting to note that the angular transition frequency ω_t increases with saturation: for instance, $\omega_t = 8.6$ Hz for $S_w = 20$ per cent, whereas $\omega_t = 11.6$ kHz at full saturation. For $S_w = 20$ per cent, the curves for Q_{Pf} and Q_S overlap, which means the attenuation is the same for both wave types. However, as saturation increases, the curve for Q_{Pf} is shifted upwards, while the curve for Q_S remains unaffected by saturation changes. For the Biot slow *P* wave, the quality factor remains constant in the viscous regime. For $f > 2\pi\omega_t$, Q_{Ps} increases with the same slope as the other volume waves. On the other hand, the EM wave quality factor is not affected by the fluid flow type but instead depends on the regime type: it has a different behaviour whether or not diffusion dominates over propagation. Q_{EM} is weak (close to 0.5) and frequency- and saturation-independent in the conduction current dominant diffusive regime, that is, at low frequencies. It increases with frequency in the displacement current dominant propagative regime, that is, for high frequencies. For simple materials, the transition frequency between both regimes is given by $f = \sigma(\omega)/(2\pi\epsilon(\omega))$ (Rubin & Hubbard 2005) and is therefore saturation-dependent.

5.3 Amplitude analysis

We also studied the amplitudes of the seismoelectric signals modelled with our programme. While it had virtually no influence on

velocities, the law chosen to compute the SPC directly influences the recovered amplitudes, which calls for a thorough comparison between the results granted by all four relations (Perrier & Morat 2000; Guichet *et al.* 2003; Revil *et al.* 2007; Allègre *et al.* 2010). Like its previous version, our modelling programme is based on the equations of Kennett & Kerry (1979), enabling to simulate the seismic and EM response of a porous tabular medium. Among other advantages, this formalism allows to boost chosen conversions by multiplying specific coefficients in the reflectivity–transmissivity matrices by arbitrary pre-factors. Multiplying the P_f-EM, S-EM and P_s-EM coefficients by an arbitrary factor of 10^8 before normalizing the corresponding electrogram by the same value allows to model the IR without the pollution of the coseismic wavefield. Using this technique, we plotted the IR maximum amplitudes against saturation S_w, for all four SPC relations (left-hand side graph in Fig. 9). It appears that using the SPC laws of Perrier & Morat (2000), Guichet *et al.* (2003) and Revil *et al.* (2007), the maximum amplitude of the IR monotonically decreases with increasing saturation. The IRs modelled using these laws reach a maximum value of about 2.5×10^{-4} V at residual saturation $S_w = 0.15$ (S_{wr}). They reach a minimum value of about 2.5×10^{-5} V at full saturation. As it could be expected, the IR follows a non-monotonic behaviour when using the relation introduced by Allègre *et al.* (2010). Its value increases from 8.8×10^{-5} V to a maximum value of 5.9×10^{-4} V when saturation increases from $S_w = 0.35$ up to a saturation close to 0.65, before decreasing with increasing saturation down to a value of 2.4×10^{-5} V

Figure 7. *P* wave, *S* wave, Biot slow wave and EM wave quality factors as a function of effective saturation S_e for the sand layer described in Table 4. These quality factors were computed at 50, 100, 150 and 200 Hz. Note that the EM wave quality factor is plotted with a linear scale.

at full saturation, about the same minimum value reached using the other laws. Therefore, the model of Allègre *et al.* (2010) returns the biggest IR amplitude of all four models (0.59 mV at $S_w = 0.65$).

In our previous work, when using the original programme to create synthetic seismoelectric recordings for full saturation conditions (Warden *et al.* 2012), we were never able to model an IR strong enough that it could be seen without subsequent filtering; we had to artificially amplify the IR with the technique mentioned above. This seemed problematic, as IRs, albeit very weak, have reportedly been measured in the field on several occasions (Haines *et al.* 2007). We thought that maybe water saturation contrasts could be responsible for the difference between the IR amplitudes measured in the field and those modelled with our original programme. To verify this hypothesis, we also plotted the coseismic surface wave mean amplitudes against saturation along with the maximum IR amplitudes (right-hand side graph in Fig. 9). It turns out that, as saturation decreases, the coseismic surface wave mean amplitude decreases for the SPC laws of Perrier & Morat (2000), Guichet *et al.* (2003) and Revil *et al.* (2007) from 1.3×10^{-2} V at full saturation, down to minimum values ranging from 8.7×10^{-6} V at $S_w = 0.15$ for the SPC derived from Revil *et al.* (2007) to 2.5×10^{-4} V for Perrier & Morat (2000). Therefore, as the water saturation falls down towards the residual saturation value S_{wr}, both the decreasing coseismic amplitudes and the increasing IR amplitudes make it progressively easier to detect the IR. For instance, according to our amplitude analysis, using the SPC derived by Revil *et al.* (2007), one may only start distinguishing the IR below $S_w = 0.35$. Modelling the

corresponding electrograms for $S_w = 0.25$ and $S_w = 0.35$ confirms this result (Fig. 10). On the other hand, the coseismic mean amplitude follows a 'bell-shaped' behaviour for the relation of Allègre *et al.* (2010): it increases from 1.3×10^{-2} V at full saturation to nearly 1.5×10^{-1} V at $S_w = 0.90$ before decreasing to 5.0×10^{-3} V at $S_w = 0.35$. In fact, for this set of parameters the IR maximum never exceeds the mean coseismic surface wave amplitude.

We also plotted the mean IR amplitude for a fixed saturation of a sand overburden ($S_w = 0.4$), whose thickness is allowed to increase from 5 to 50 m (Fig. 11). Quite unsurprisingly, the mean IR amplitude decreases with increasing thickness, mainly because the distance between the interface and the surface-located receivers increases. For instance, for the SPC law of Guichet *et al.* (2003) it decreases from 2.5×10^{-3} V at a depth of 5 m down to 9.3×10^{-6} V at a depth of 50 m. It turns out that, for shallow horizons, a change in the interface depth by only a few metres may modify the IR by an order of magnitude.

6 CAPILLARY FRINGE BETWEEN A SATURATED SAND HALF-SPACE AND A PARTIALLY SATURATED SAND OVERBURDEN

6.1 Model description

The simple subsurface layered models considered up to this point all simulate sharp saturation contrasts between consecutive units
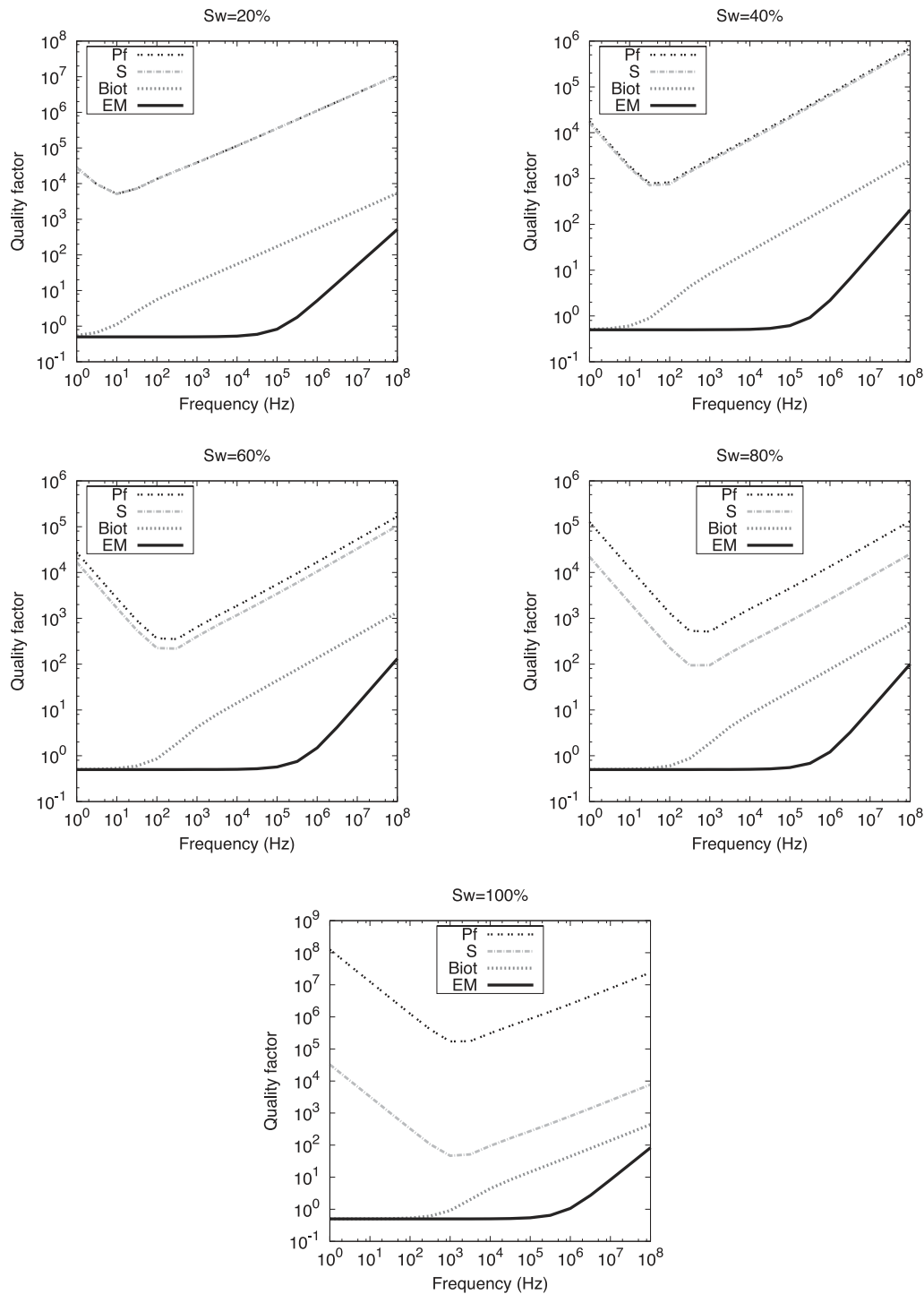
Figure 8. Seismic and electromagnetic quality factors versus frequency for 20, 40, 60, 80 and 100 per cent water saturation.

(Fig. 12a). In reality, instead of jumping from one value to the other, saturation may smoothly decrease with distance to the water table, due to capillary action. We use the partial saturation modelling programme to simulate such a capillary fringe between vadose and saturated sand layers (Table 5) by modelling a great number of very thin layers whose saturation increases by a small constant step from one layer to the other (Fig. 12b). In doing this, we adopt the definition according to which the unsaturated zone includes the capillary fringe: other authors may prefer to define the capillary fringe as being part of the saturated zone. We model here 100

layers, 0.5 cm thick, which saturation increases by $S_w = 0.5$ per cent from one layer to the next. The overburden has a water saturation of 50 per cent, while the fully saturated half-space simulates an aquifer ($S_w = 1$). The thickness of the capillary fringe is controlled by the pore sizes; it is generally less for coarse-grain materials than for fine-grain materials (Kaufman *et al.* 2011). As it was reported to be less than 1 m thick in sands (Walker 2012), we chose to work with a capillary zone 0.5 m thick, embedded between 29.5 and 30 m. Seismic and seismoelectromagnetic waves are generated by a vertical source of peak frequency $f_{\text{peak}} = 120$ Hz, buried 3 m deep,
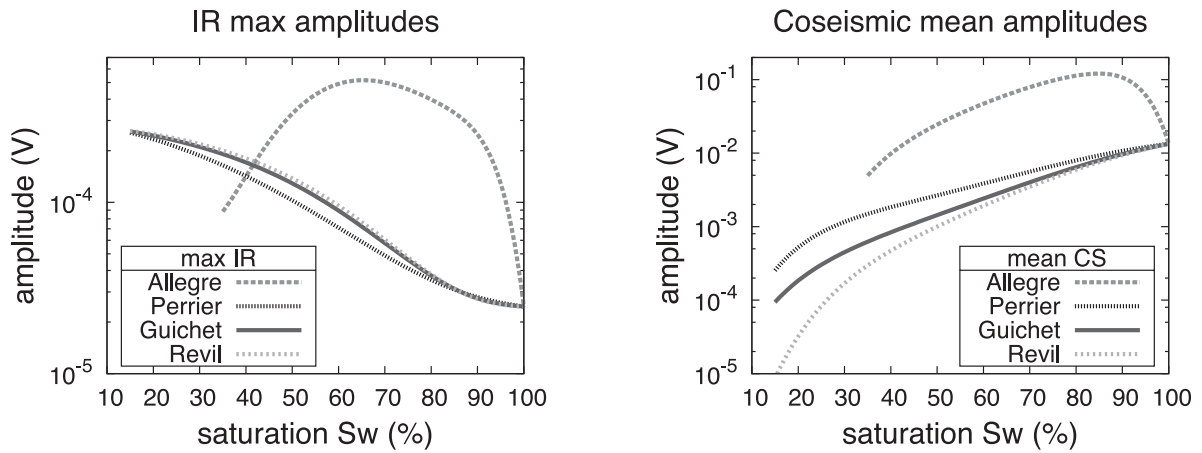
Figure 9. Interface response maximum amplitude and coseismic mean amplitude values versus saturation using the SPC derived by Perrier & Morat (2000), Guichet *et al.* (2003), Revil *et al.* (2007) and Allègre *et al.* (2010).
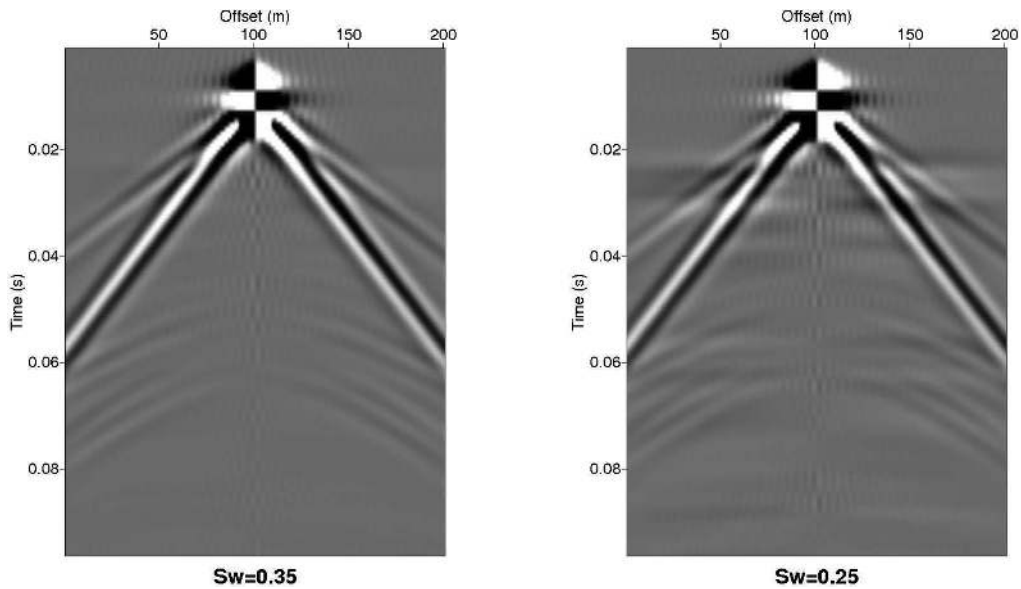

Figure 10. Horizontal electric field generated with our modelling code for the SPC derived by Revil *et al.* (2007) for $S_w = 0.35$ and $S_w = 0.25$. As one could deduce from Fig. 9, the interface response at 0.020 s can be distinguished when S_w falls below 0.35.

and recorded by 201 receivers evenly spaced between $x = -50$ and 50 m.

6.2 Influence of the capillary fringe on the IR

We compared the horizontal electric field E_x generated both for a subsurface model exhibiting a sharp saturation contrast between the vadose and saturated sand layers (Fig. 12a) and a model including a capillary fringe (Fig. 12b). To recover the IR free from the co-seismic waves, we proceeded as in Section 5.3, by multiplying the P_f-EM, S-EM and P_s-EM coefficients by an arbitrary factor before normalizing the resulting electrograms by the same value. Both seismoelectric recordings appear very similar (Fig. 13). They exhibit a first event of zero moveout around 45 ms, a time corresponding to the sum of the traveltime needed by the fast P wave to go from the source to the interface and for the converted EM wave to travel back to the receivers deployed at the ground surface. A second 'flat' event of lower magnitude appears around 68 ms: it corresponds to the converted S-EM wave.

Although the IRs modelled with or without a capillary fringe closely resemble each other, their amplitudes are very different. We have computed the IR mean amplitude versus offset over a 25 samples window centred on the P_f-EM conversion (Fig. 13a) and the S-EM conversion (Fig. 13b). The P_f-EM IR obtained by modelling a capillary fringe consisting of 100 layers appears roughly 2.5 times weaker than the IR recovered by simulating a simple contact (Fig. 14): for a simple contact, the P_f-EM IR mean amplitude at offset $x = 15$ m is 3.4×10^{-5} V, versus only 1.3×10^{-5} V for a 100 layers capillary fringe model. Modelling other capillary fringes using a smaller number of layers (e.g. 10 or 50 layers) yields the same result. On the other hand, the S-EM IR obtained for a tabular model including a capillary fringe is slightly stronger than the IR recovered for a simple contact between the vadose and saturated sand layers (4.5×10^{-6} V versus 4.0×10^{-6} V at offset $x = 12$ m). These results suggest that it would be harder to measure such an IR for a smooth saturation transition at the top of the water table than for a sharp saturation contrast between the vadose and saturated zones.

IR mean amplitudes vs Depth
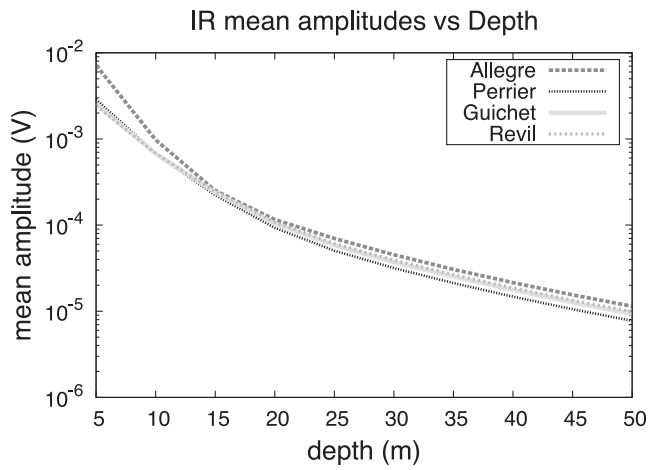
Figure 11. Interface response maximum amplitude values in the sand overburden as a function of the depth of the interface between the unsaturated sand layer ($S_w = 40$ per cent) and the fully saturated sandstone half-space. These results were modelled for the SPC laws of Perrier & Morat (2000), Guichet *et al.* (2003), Revil *et al.* (2007) and Allègre *et al.* (2010).

7 CONCLUSION

In this paper, we extended Pride's theory originally developed to simulate seismoelectromagnetic wave conversions in fully saturated porous media to partial saturation conditions. To achieve this goal, mechanical, EM and coupling constitutive properties were computed for a water/air mixture. In particular, a generalization of Biot–Gassmann theory to the unsaturated case was performed through a simple homogenization technique. For the EM properties, we used the CRIM formula to determine the effective fluid permittivity and an extension of Pride's equation to compute the conductivity of the fluid in unsaturated rocks. The saturation-dependent electrokinetic coupling was tested using various laws experimentally derived to describe the behaviour of the SPC against water saturation. These changes have been incorporated into an existing seismoelectromagnetic wave propagation algorithm, originally developed to study seismoelectric properties in saturated stratified media. This new code is used to model the seismoelectric response of a simple tabular medium for which the saturation in the sand overburden is allowed to vary, while remaining constant in the underlying sandstone half-space. A thorough amplitude analysis reveals that, using

Table 5. Properties of the model described in Section 6.

|	Sand overburden	Sand half-space
ϕ	35	35
c_s	20	20
m	2.05	2.05
k_0 (m^2)	10^{-11}	10^{-11}
k_s (Pa)	35×10^9	35×10^9
G_s (Pa)	44×10^9	44×10^9
k_f (Pa)	2.27×10^9	2.27×10^9
k_{fr} (Pa)	2.84×10^9	2.84×10^9
G_{fr} (Pa)	2.49×10^9	2.49×10^9
η_w (Pa s)	1×10^{-3}	1×10^{-3}
η_g (Pa s)	1.8×10^{-5}	1.8×10^{-5}
ρ_s (kg m^{-3})	2.6×10^3	2.6×10^3
ρ_w (kg m^{-3})	1×10^3	1×10^3
ρ_g (kg m^{-3})	1	1
C_0 (mol L^{-1})	1×10^{-3}	1×10^{-3}
σ (S m^{-1})	3.22×10^{-4}	1.32×10^{-3}
ζ (V)	-0.065	-0.065
κ_w	80	80
κ_s	4	4
κ_g	1	1
T (K)	298	298
S_w	0.5	1

the SPC laws of Perrier & Morat (2000), Guichet *et al.* (2003) and Revil *et al.* (2007), the amplitude ratio between the IR and the coseismic signal increases with decreasing water saturation of the shallow sandy layer. For instance, the IR maximum amplitude at full saturation is three orders of magnitude smaller than the coseismic mean amplitude, using the SPC law derived by Perrier & Morat (2000), which means that, for fully saturated media, the IR is very difficult to detect. On the other hand, using the same SPC law under residual saturation conditions, the IR maximum amplitude is five times greater than the coseismic mean amplitude. Therefore, an IR created by a saturation contrast may be easier to detect than a seismoelectric conversion occurring at the boundary between two fully saturated units. This result accounts for the amplitude contrasts between the IRs and the coseismic signals observed in the field over unsaturated environments, which could not be explained using the original version of the code, allowing to model only saturated conditions. On the other hand, the non-monotonic SPC law of Allègre
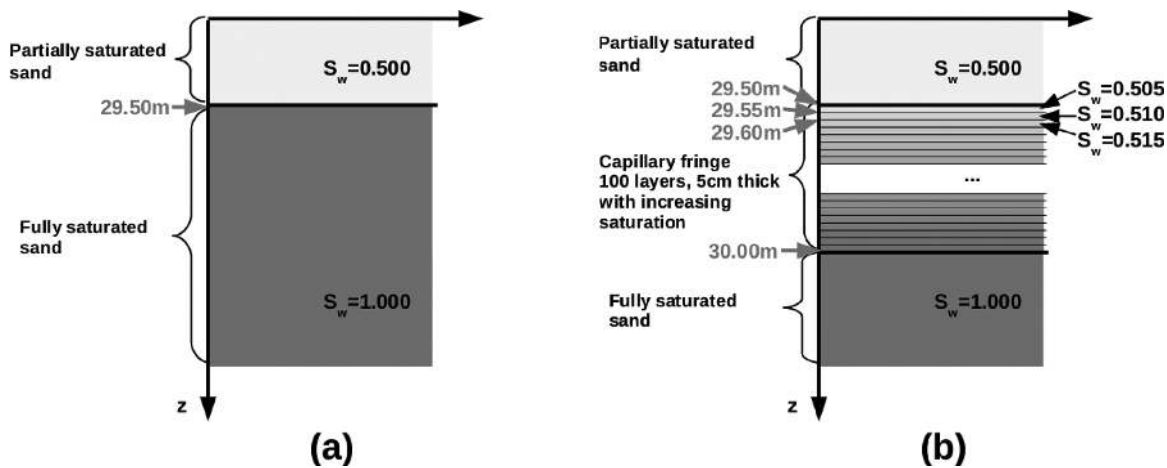
Figure 12. Tabular models used to simulate (a) a simple contact between a shallow unsaturated sand layer and a saturated sand half-space and (b) a capillary fringe between these two units. The capillary fringe is modelled by 100 thin unsaturated layers, 0.5 cm thick, which saturation increases with depth with a step of $S_w = 0.5$ per cent between two consecutive layers.
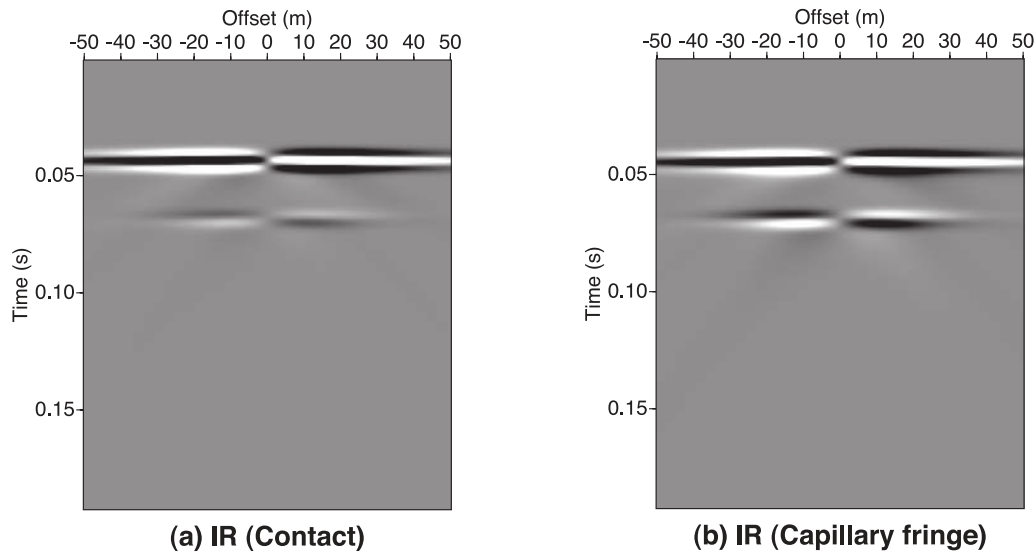
Figure 13. Interface responses modelled for (a) a simple contact between a shallow unsaturated sand layer and a saturated sand half-space and (b) a capillary fringe between these two units (see Fig. 12). The SPC law of Revil *et al.* (2007) was used here.
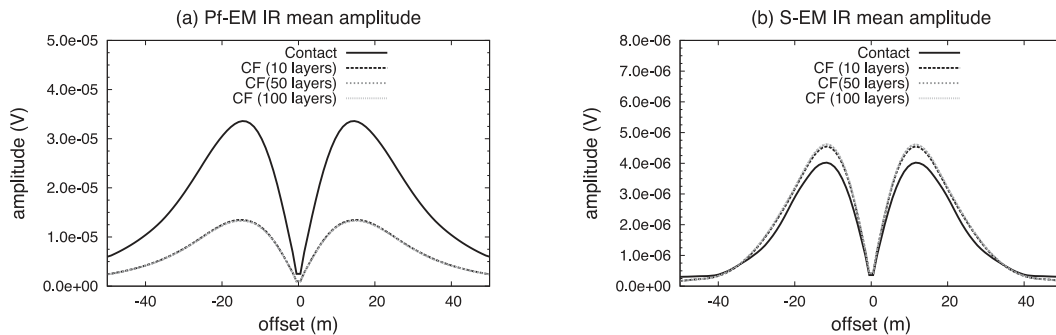
Figure 14. Interface Response mean amplitude distribution as a function of offset, for a simple contact (solid black line) and for several capillary models designed with a different numbers of layers (grey broken lines). (a) P_f-EM conversion. (b) S-EM conversion. The SPC law of Guichet *et al.* (2003) was used here. For the P_f-EM conversion, the models including a capillary fringe yield lower IR amplitudes than the model with a sharp saturation contrast.

et al. (2010) yields a greater maximum IR amplitude than the other three models: this maximum IR amplitude is reached at a saturation of $S_w = 0.65$. Furthermore, our extended programme is also used to model a capillary fringe at the top of a water table. This study suggests that such a smooth saturation transition may be harder to detect than a sharp saturation contrast between two consecutive layers, as P_f-EM IR amplitudes recovered for subsurface models including a capillary zone appear smaller than for models exhibiting a sharp contrast. On the other hand, S-EM IRs seem slightly stronger for capillary fringe models than for sharp saturation contrasts. This result suggests that seismoelectric imaging using S-wave sources may allow to detect smooth saturation transition zones.

Our developments open the possibility for further investigations beyond the scope of this paper. In future work, one should attempt to simulate seismoelectric wave propagation in complex multiphasic porous media with gas/brine or oil/brine mixtures filling the pore space. In this case, one would need to find another way to derive the saturation-dependent seismoelectric coupling $L_0(S_w)$ in the other mixtures, which may imply using other laws describing the SPC behaviour for complex multiphasic fluids (Moore *et al.* 2004; Jackson 2010). Moreover, our programme will be able to model a wide variety of environments, such as temperate glaciers (Kulessa *et al.* 2006). Finally, future studies about the transfer functions under unsaturated conditions are also needed and will be possible using our developments.

REFERENCES

Allègre, V., Jouniaux, L., Lehmann, F. & Sailhac, P., 2010. Streaming potential dependence on water-content in Fontainebleau sand, *Geophys. J. Int.,* **182,** 1248–1266.

Allègre, V., Lehmann, F., Ackerer, P., Jouniaux, L. & Sailhac, P., 2012. A 1D modelling of streaming potential dependence on water content during drainage experiment in sand, *Geophys. J. Int.,* **189**(1), 285–295.

Allen, T., 1996. *Particle Size Measurement: Surface Area and Pore Size Determination,* Springer Verlag, New York.

Bard, A.J. & Faulkner, L.R., 2001. *Electrochemical Methods: Fundamentals and Applications,* John Wiley and Sons, New York.

Barrière, J., Bordes, C., Brito, D., Sénéchal, P. & Perroud, H., 2012. Laboratory monitoring of *P*-waves in partially saturated sand, *Geophys. J. Int.,* **191**(3), 1152–1170.

Batzle, M.L. & Wang, Z., 1992. Seismic properties of pore fluids, *Geophysics,* **57**(11), 1396–1408.

Biot, M.A., 1956a. Theory of propagation of elastic waves in a fluid-saturated porous solid: I. Low frequency range, *J. acoust. Soc. Am.,* **28**(2), 168–178.

Biot, M.A., 1956b. Theory of propagation of elastic waves in a fluid-saturated porous solid: II. High frequency range, *J. acoust. Soc. Am.,* **28**(2), 178–191.

Birchak, J., Gardner, C., Hipp, J. & Victor, J., 1974. High dielectric constant microwave probes for sensing soil moisture, *Proc. IEEE,* **62**(1), 93–98.

Block, G.I. & Harris, J.G., 2006. Conductivity dependence of seismoelectric wave phenomena in fluid-saturated sediments, *J. geophys. Res.,* **111**, B01304, doi:10.1029/2005JB003798.

Bordes, C., Garambois, S., Jouniaux, L. & Senechal, P., 2009. Seismoelectric measurements for the characterization of partially saturated porous media, *American Geophysical Union, Fall Meeting 2009,* abstract #NS31B-1161.

Bordes, C., Jouniaux, L., Garambois, S., Dietrich, M., Pozzi, J.-P. & Gaffet, S., 2008. Evidence of the theoretically predicted seismo-magnetic conversion, *Geophys. J. Int.,* **174**, 489–504.

Brie, A., Pampuri, F., Marsala, A. & Meazza, O., 1995. Shear sonic interpretation in Gas-Bearing sands, in *Proceedings of the Annual Technical Conference and Exhibition,* Society of Petroleum Engineers, paper 30595-MS.

Brovelli, A., Cassiani, G., Dalla, E., Bergamini, F., Pitea, D. & Binley, A.M., 2005. Electrical properties of partially saturated sandstones: novel computational approach with hydrogeophysical applications, *Water Resour. Res.,* **41**(3), doi:10.1029/2004WR003628.

Butler, K.E., 1993. Subtraction of powerline harmonics from geophysical records, *Geophysics,* **58**(6), 898–903.

Butler, K.E., 1996. Measurement of the seismoelectric response from a shallow boundary, *Geophysics,* **61**(6), 1769–1778.

Butler, K.E. & Russell, R.D., 2003. Cancellation of multiple harmonic noise series in geophysical records, *Geophysics,* **68**(3), 1083–1090.

Cadoret, T., Marion, D. & Zinszner, B., 1995. Influence of frequency and fluid distribution on elastic wave velocities in partially saturated limestones, *J. geophys. Res.,* **100**(B6), 9789–9803.

Carcione, J., Picotti, S., Gei, D. & Rossi, G., 2006. Physics and seismic modeling for monitoring CO_2 storage, *Pure appl. Geophys.,* **163**(1), 175–207.

Chapman, D.L., 1913. A Contribution to the Theory of Electrocapillarity, *Phil. Mag.,* **25**(6), 475–481.

Chen, B. & Mu, Y., 2005. Experimental studies of seismoelectric effects in fluid-saturated porous media, *J. geophys. Eng.,* **2**, 222–230.

Davis, J.A., James, R.O. & Leckie, J., 1978. Surface ionization and complexation at the Oxide/water interface, *J. Colloid Interface Sci.,* **63**, 480–499.

Dukhin, S.S. & Derjaguin, B.V., 1974. *Surface and Colloid Science,* ed. Matijevic, E., John Wiley and Sons, New York.

Dupuis, J.C. & Butler, K.E., 2006. Vertical seismoelectric profiling in a borehole penetrating glaciofluvial sediments, *Geophys. Res. Lett.,* **33**, L16301, doi:10.1029/2006GL026385.

Dupuis, J.C., Butler, K.E. & Kepic, A.W., 2007. Seismoelectric imaging of the vadose zone of a sand aquifer, *Geophysics,* **72**(6), A81–A85.

Dupuis, J.C., Butler, K.E., Kepic, A.W. & Harris, B.D., 2009. Anatomy of a seismoelectric conversion: measurements and conceptual modeling in boreholes penetrating a sandy aquifer, *J. geophys. Res.,* **114**, B10306, doi:10.1029/2008JB005939.

Dupuy, B., De Barros, L., Garambois, S. & Virieux, J., 2011. Wave propagation in heterogeneous porous media formulated in the frequency-space domain using a discontinuous Galerkin method, *Geophysics,* **76**(4), N13–N28.

Dvorkin, J. & Nur, A., 1998. Acoustic signatures of patchy saturation, *Int. J. Solids Struct.,* **35**(34–35), 4803–4810.

Frenkel, J., 1944. On the theory of seismic and electroseismic phenomena in a moist soil, *J. Phys.,* **8**(4), 230–241.

Garambois, S. & Dietrich, M., 2001. Seismoelectric wave conversions in porous media: field measurements and transfer function analysis, *Geophysics,* **66**(5), 1417–1430.

Garambois, S. & Dietrich, M., 2002. Full waveform numerical simulations of seismoelectromagnetic wave conversions in fluid-saturated stratified porous media, *J. geophys. Res.,* **107**, B72148, doi:10.1029/2001JB000316.

Garambois, S., Sénéchal, P. & Perroud, H., 2002. On the use of combined geophysical methods to assess water content and water conductivity of near-surface formations, *J. Hydrol.,* **259**(1–4), 32–48.

Glover, P.W.J., Walker, E. & Jackson, M.D., 2012. Streaming-potential coefficient of reservoir rock: a theoretical model, *Geophysics,* **77**(2), D17–D43.

Gomaa, M.M.N.R.C., 2008. Relation between electric properties and water saturation for hematitic sandstone with frequency, *Ann. Geophys.,* **51**, 801–811.

Gouy, G.L., 1910. Sur la constitution de la charge électrique à la surface d'un électrolyte, *Journal de Physique Théorique et Appliquée,* **9**(4), 457–468.

Gueguen, Y. & Palciauskas, V., 1994. *Introduction to the Physics of Rocks,* Princeton University Press, Princeton.

Guichet, X., Jouniaux, L. & Pozzi, J., 2003. Streaming potential of a sand column in partial saturation conditions, *J. geophys. Res.,* **108**, B32141, doi:10.1029/2001JB001517.

Haartsen, M.W. & Pride, S.R., 1997. Electroseismic waves from point sources in layered media, *J. geophys. Res.,* **102**(B11), 24 745–24 769.

Haines, S.S. & Pride, S.R., 2006. Seismoelectric numerical modeling on a grid, *Geophysics,* **71**(6), N57–N65.

Haines, S.S., Pride, S.R., Klemperer, S.L. & Biondi, B., 2007. Seismoelectric imaging of shallow targets, *Geophysics,* **72**(2), G9–G20.

Hu, H., Guan, W. & Harris, J.M., 2007. Theoretical simulation of electroacoustic borehole logging in a fluid saturated porous formation, *J. acoust. Soc. Am.,* **122**(1), 135–145.

Hunt, C.W. & Worthington, M.H., 2000. Borehole electrokinetic responses in fracture dominated hydraulically conductive zones, *Geophys. Res. Lett.,* **27**(9), 1315–1318.

Jackson, M.D., 2010. Multiphase electrokinetic coupling: insights into the impact of fluid and charge distribution at the pore scale from a bundle of capillary tubes model, *J. geophys. Res.,* **115**, B07206, doi:10.1029/2009JB007092.

Jardani, A., Revil, A., Slob, E. & Söllner, W., 2010. Stochastic joint inversion of 2D seismic and seismoelectric signals in linear poroelastic materials: a numerical investigation, *Geophysics,* **75**(1), N19–N31.

Johnson, D.L., Koplik, J. & Dashen, R., 1987. Theory of dynamic permeability in fluid saturated porous media, *J. Fluid. Mech.,* **176**, 379–402.

Jouniaux, L. & Bordes, C., 2012. Frequency-dependent streaming potentials: a review, *Int. J. Geophys.*

Jouniaux, L. & Ishido, T., 2012. Electrokinetics in Earth Sciences: a tutorial, *Int. J. Geophys.,* **2012,** doi:10.1155/2012/286107.

Kaufman, M.M., Rogers, D.T. & Murray, K.S., 2011. *Urban Watersheds: Geology, Contamination, and Sustainable Development,* CRC Press, Boca Raton.

Kennett, B.L.N. & Kerry, N.J., 1979. Seismic waves in a stratified half space, *Geophys. J. Int.,* **57**(3), 557–583.

Knight, R. & Dvorkin, J., 1992. Seismic and electrical properties of sandstones at low saturations, *J. geophys. Res.,* **97**, 17 425–17 432.

Knight, R. & Nolen-Hoeksema, R., 1990. A laboratory study of the dependence of elastic wave velocities on pore scale fluid distribution, *Geophys. Res. Lett.,* **17**, 1529–1532.

Knight, R.J., 1984. *The dielectric constant of sandstones, 5 Hz to 13 MHz, PhD thesis,* Stanford University.

Knight, R.J. & Nur, A., 1987. The dielectric constant of sandstones, 60 kHz to 4 MHz, *Geophysics,* **52**, 644–654.

Kröger, B. & Kemna, A., 2012. Anatomical and morphogenetic analysis of seismoelectric conversion patterns at geological units, in *Proceedings of the EGU General Assembly Conference Abstracts,* vol. 14, EGU, Munich p. 1676.

Kulessa, B., Murray, T. & Rippin, D., 2006. Active seismoelectric exploration of glaciers, *Geophys. Res. Lett.,* **33**, L07503, doi:10.1029/2006GL025758.

Mavko, G., Mukerji, T. & Dvorkin, J., 2009. *The Rock Physics Handbook: Tools for Seismic Analysis of Porous Media,* Cambridge University Press, Cambridge.

Mikhailov, O.V., Queen, J. & Toksöz, M.N., 2000. Using borehole electroseismic measurements to detect and characterize fractured (permeable) zones, *Geophysics,* **65**(4), 1098–1112.

Moore, J.F., Glaser, S.D. & Morrison, H.F., 2004. The streaming potential of liquid carbon dioxide in Berea sandstone, *Geophys. Res. Lett.,* **31,** L17610, doi:10.1029/2004GL020774.

Müller, T.M., Gurevich, B. & Lebedev, M., 2010. Seismic wave attenuation and dispersion resulting from wave-induced flow in porous rocks—a review, *Geophysics,* **75**(5), 75A147–75A164.

Neev, J. & Yeatts, F.R., 1989. Electrokinetic effects in fluid-saturated poroelastic media, *Phys. Rev. B,* **13,** 9135–9141.

Overbeek, J.T.G., 1952. Electrochemistry of the double layer, in *Colloid Science, Irreversible Systems,* Vol. 1, pp. 115–193, ed. Kruyt, H.R., Elsevier, Amsterdam.

Perrier, F. & Morat, P., 2000. Characterization of electrical daily variations induced by capillary flow in the non-saturated zone, *Pure appl. Geophys.,* **157**(5), 785–810.

Plug, W.-J., Slob, E., van Turnhout, J. & Bruining, J., 2007. Capillary pressure as a unique function of electric permittivity and water saturation, *Geophys. Res. Lett.,* **34**(13), doi:10.1029/2007GL029674.

Pride, S., 1994. Governing equations for the coupled electromagnetics and acoustics of porous media, *Phys. Rev. B,* **50**(21), 15 678–15 696.

Pride, S. & Morgan, F.D., 1991. Electrokinetic dissipation induced by seismic waves, *Geophysics,* **56**(7), 914–925.

Pride, S.R., 2005. *Relationships between Seismic and Hydrological Properties,* Vol. 50, Springer, Netherlands.

Pride, S.R. & Haarsten, M.W., 1996. Electroseismic wave properties, *J. acoust. Soc. Am.,* **100**(3), 1301–1315.

Ren, H., Chen, X. & Huang, Q., 2012. Numerical simulation of coseismic electromagnetic fields associated with seismic waves due to finite faulting in porous media, *Geophys. J. Int.,* **188**(3), 925–944.

Reppert, P.M., Morgan, F.D., Lesmes, D.P. & Jouniaux, L., 2001. Frequency-dependent streaming potentials, *J. Colloid Interface Sci.,* **234,** 194–203.

Revil, A. & Linde, N., 2006. Chemico-electromechanical coupling in microporous media, *J. Colloid Interface Sci.,* **302**(2), 682–694.

Revil, A., Linde, N., Cerepi, A., Jougnot, D., Matthäi, S. & Finsterle, S., 2007. Electrokinetic coupling in unsaturated porous media, *J. Colloid Interface Sci.,* **313**(1), 315–327.

Ritchey, J.D. & Rumbaugh, J.O., 1996. *Subsurface Fluid Flow (Ground-Water and Vadose Zone) Modeling,* ASTM, West Conshohocken.

Rubin, Y. & Hubbard, S.S., 2005. *Hydrogeophysics,* Springer, Berlin.

Schakel, M.D., Smeulders, D.M.J., Slob, E.C. & Heller, H.K.J., 2011. Seismoelectric interface response: experimental results and forward model, *Geophysics,* **76**(4), N29–N36.

Schakel, M.D., Smeulders, D.M.J., Slob, E.C. & Heller, H.K.J., 2012. Seismoelectric fluid/porous-medium interface response model and measurements, *Transp. Porous media,* **93,** 271–282.

Schoemaker, F.C., Smeulders, D.M.J. & Slob, E.C., 2007. Simultaneous determination of dynamic permeability and streaming potential, *SEG Expanded Abstr.,* **26**(1), 1555–1559.

Singarimbun, A., Mahardika, H., Srigutomo, W. & Fauzi, U., 2008. A preliminary result of seismoelectric responses study on shallow fluid-saturated layer: numerical modeling using transfer function approach, *Indonesian J. Phys.,* **19**(3), 61–68.

Singer, J., Saunders, J., Holloway, L., Stoll, J.B., Pain, C., Stuart-Bruges, W. & Mason, G., 2005. Electrokinetic logging has the potential to measure the permeability, in *Society of Petrophysicists and Well Log Analysts, 46th Annual Logging Symposium.*

Stern, O., 1924. Zur Theorie der elektrolytischen Doppelschicht, *Z. Electrochem.,* **30,** 508–516.

Strahser, 2007. Polarisation and slowness of seismoelectric signals: a case study, *Near Surf. Geophys,* **5,** 97–114.

Strahser, M., Jouniaux, L., Sailhac, P., Matthey, P. & Zillmer, M., 2011. Dependence of seismoelectric amplitudes on water content, *Geophys. J. Int.,* **187**(3), 1378–1392.

Teja, A.S. & Rice, P., 1981. Generalized corresponding states method for the viscosities of liquid mixtures, *Ind. Eng. Chem. Fund.,* **20**(1), 77–81.

Thompson, A.H. & Gist, G.A., 1993. Geophysical applications of electrokinetic conversion, *The Leading Edge,* **12**(12), 1169–1173.

Thompson, A.H. *et al.*, 2005. Field tests of electroseismic hydrocarbon detection, *Geophysics,* **72,** 565–568.

Thompson, A.H., Sumner, J.R. & Hornbostel, S.C., 2007. Electromagnetic-to-seismic conversion, *Leading Edge,* **26**(4), 428–435.

Toksöz, M.N. & Zhu, Z., 2005. Seismoelectric and seismomagnetic measurements in fractured borehole models, *Geophys.,* **70**(4), F45–F51.

Vinogradov, J. & Jackson, M., 2011. Multiphase streaming potential in sandstones saturated with gas/brine and oil/brine during drainage and imbibition, *Geophys. Res. Lett.,* **38,** L01301, doi:10.1029/2010GL045726.

Walker, M., ed., 2012. *Hot Deserts: Engineering, Geology and Geomorphology: Engineering Group Working Party Report,* Geological Society.

Warden, S., Garambois, S., Sailhac, P., Jouniaux, L. & Bano, M., 2012. Curvelet-based seismoelectric data processing, *Geophys. J. Int.,* **190,** 1533–1550.

White, J.E., 1975. Computed seismic speeds and attenuation in rocks with partial gas saturation, *Geophysics,* **40**(2), 224–232.

Yamazaki, K., 2012. Estimation of temporal variations in the magnetic field arising from the motional induction that accompanies seismic waves at a large distance from the epicentre, *Geophys. J. Int.,* **190,** 1393–1403.

Zhu, Z. & Toksöz, M.N., 2003. Crosshole seismoelectric measurements in borehole models with fractures, *Geophysics,* **68**(5), 1519–1524.

Zhu, Z., Haartsen, M.W. & Toksöz, M.N., 1999. Experimental studies of electrokinetic conversions in fluid-saturated borehole models, *Geophysics,* **64,** 1349–1356.

Zyserman, F.I., Gauzellino, P.M. & Santos, J.E., 2010. Finite element modeling of SHTE and PSVTM electroseismics, *J. appl. Geophys.,* **72**(2), 79–91.

SUPPORTING INFORMATION

Additional Supporting Information may be found in the online version of this article:

Figure S1. Dielectric constant versus water saturation S_w as measured by Knight (1984) on Berea ($\phi = 19.7$ per cent) sandstone samples and Gomaa (2008) for Aswan ($\phi = 23$ per cent) sandstone. The dielectric constant computed with the CRIM formula for a sandstone ($\phi = 23$ per cent) is also plotted for comparison.
Figure S2. Results of the reciprocity test described in subsection 1.2 (http://gji.oxfordjournals.org/lookup/suppl/doi:10.1093/gji/ggt198 /-/ DC1).

Please note: Oxford University Press are not responsible for the content or functionality of any supporting materials supplied by the authors. Any queries (other than missing material) should be directed to the corresponding author for the article.